



Systematic assessment of the diabatic processes that modify low-level potential vorticity in extratropical cyclones

Roman Attinger¹, Elisa Spreitzer¹, Maxi Boettcher¹, Heini Wernli¹, and Hanna Joos¹

¹Institute for Atmospheric and Climate Science, ETH Zurich, Switzerland

Correspondence: Roman Attinger (roman.atinger@env.ethz.ch)


Abstract. Diabatic processes significantly affect the development and structure of extratropical cyclones. Previous studies quantified the dynamical relevance of selected diabatic processes by studying their influence on potential vorticity (PV) in individual cyclones. However, a more general assessment of the relevance of all PV-modifying processes in a larger ensemble of cyclones is currently missing. Based on a series of twelve 35-day model simulations using the Integrated Forecasting System (IFS) of the European Centre for Medium-range Weather Forecasts (ECMWF), this study systematically quantifies the relevance of individual diabatic processes for the dynamics of 288 rapidly intensifying extratropical cyclones. To this end, PV tendencies associated with each parametrized process in the model are accumulated along 15 h backward trajectories. The investigation focuses on regions of high PV (≥ 1 PVU) along the cold front, warm front, and in the cyclone center, as well as of negative PV (≤ -0.1 PVU) along the cold and warm front in the lower troposphere.

On average, the primary processes that modify PV during the 24 h period of most rapid cyclone intensification remain temporally consistent for all anomalies considered. However, a pronounced case-to-case variability is found when comparing the dominant processes across individual cyclones. Along the cold front, PV is primarily generated by condensation in half of the investigated cyclones. For the remaining cyclones, convection or long-wave radiative cooling become the dominant process depending on environmental conditions. Results are similar for both seasons with a reduced role of convection for the generation of PV along the cold front in the warm season. Negative PV west of the cold front is produced by turbulent exchange of momentum and temperature as well as long-wave radiative heating. The relevance of long-wave radiative heating is reduced during summer. The positive PV anomaly at the warm front is predominantly generated by condensation in the cold season, whereas turbulent mixing becomes the prevalent process during the warm season. Convection only plays a minor role for the generation of PV at the warm front. Negative PV along the warm front is produced by long-wave radiative heating, turbulent temperature tendencies, or melting of snow in the cold season. Turbulent temperature tendencies become the dominant process decreasing PV at the warm front in the warm season, together with melting of snow and turbulent exchange of momentum. The positive PV anomaly in the cyclone center is primarily produced by condensation, with only few cyclones where PV production is mainly associated with turbulent mixing or convection.

A composite analysis further reveals that PV anomalies generated by convection require a negative air-sea temperature difference in the warm sector of the cyclone, which promotes a heat flux directed into the atmosphere and destabilizes the boundary layer. These cyclones primarily occur over warm ocean currents in the cold season. On the other hand, cyclones that occur in a significantly colder environment are often associated with a positive air-sea temperature difference in the warm



sector, leading to PV generation by long-wave radiative cooling. Finally, long-wave radiative heating due to a negative air-sea temperature difference in the cold sector can produce negative PV along the cold and warm front.

30 The general agreement between accumulated PV tendencies and the net PV change along trajectories is good. Therefore, the approach used in this study yields valuable insight regarding the specific physical processes that modify low-level PV in rapidly deepening extratropical cyclones 

1 Introduction

Sub-grid scale physical processes such as cloud microphysics, radiation, and turbulence can substantially influence the life cycle of extratropical cyclones (e.g. Kuo et al., 1991). Previous studies highlight a considerable contribution of condensational heating to the cyclonic circulation of extratropical cyclones (e.g. Davis and Emanuel, 1991; Stoelinga, 1996), thereby aiding in the intensification of these weather systems. Other microphysical processes including evaporation, melting, or sublimation of hydrometeors also have the potential to influence the frontal circulation (Huang and Emanuel, 1991; Szeto and Stewart, 1997; Igel and v. d. Heever, 2014) and the development of extratropical cyclones (Joos and Wernli, 2012; Dearden et al., 2016; Hardy et al., 2017). Furthermore, turbulence (Tory and Reeder, 2005; Adamson et al., 2006) and air-surface interactions (Muir and Reeder, 2010) can also modify the structure and evolution of cyclones and their accompanying fronts.

Studies about the role of diabatic processes for the development of extratropical cyclones frequently adopt the potential vorticity (PV) framework (Hoskins et al., 1985). PV combines information on the static stability and circulation of the atmosphere and is conserved following an air parcel in a frictionless and adiabatic flow (Rossby, 1940; Ertel, 1942). The distribution of PV is essential for the evolution of Rossby waves and surface cyclones. Since material changes in PV are directly linked to latent heating and frictional acceleration, this characteristic can be exploited to identify the physical processes that modify PV.

Applying the PV framework to observed extratropical cyclones revealed that intense mid-level latent heating produces a low-level PV maximum, which enhances the coupling of the lower- and upper-level wave (Manabe, 1956; Davis, 1992; Stoelinga, 1996). The majority of extratropical cyclones feature a coherent airstream, which rapidly ascends ahead of the cold front in the warm sector (Green et al., 1966; Harrold, 1973; Browning et al., 1973). This so-called warm conveyor belt (WCB) is generally considered to be the primary precipitating airstream in extratropical cyclones (Browning, 1990) and produces an intense low-level PV maximum (Wernli and Davies, 1997; Joos and Wernli, 2012; Binder et al., 2016). In more detail, Chagnon et al. (2013) found that condensational heating along the WCB and evaporative cooling towards the cold air enhances PV along the cold front and reduces PV behind the front. They argued that the PV production at the front enhances the poleward flow in the warm sector, in agreement with Lackmann (2002). Additionally, snow sublimation was found to decrease PV north of the warm front in both an idealized baroclinic wave simulation (Crezee et al., 2017) and in a real-case simulation of a North Pacific cyclone (Attinger et al., 2019).

Frictional processes also substantially modify the low-level PV distribution in extratropical cyclones. In general, friction reduces the growth rate of baroclinic disturbances (Valdes and Hoskins, 1988) by reducing the coupling between the upper and lower levels (Adamson et al., 2006), forcing for ascent, and convergence through Ekman pumping (Beare, 2007; Boutle



et al., 2015). Conversely, a few studies described the frictional generation of PV along the warm front, which might contribute to an intensification of extratropical cyclones (Stoelinga, 1996; Adamson et al., 2006; Plant and Belcher, 2007; Attinger et al., 2019). Moreover, the interaction of orographically generated low-level PV bands with an upper-level trough can lead to lee cyclogenesis (Aebischer and Schär, 1998).

65 Finally, diabatic cooling of the warm sector by latent and sensible heat fluxes directed into the ocean was found to increase the stratification of the marine boundary layer, thereby enhancing low-level PV along the cold front in a North Atlantic (Neiman et al., 1990) and North Pacific (Attinger et al., 2019) cyclone. On the other hand, low-level PV is generally reduced in the cold sector of extratropical cyclones, where the comparatively warm ocean destabilizes the boundary layer through surface sensible heat fluxes directed into the atmosphere (Chagnon et al., 2013; Vannière et al., 2016).

70 Despite great efforts in improving the understanding of diabatic processes (e.g. Vaughan et al., 2015), their correct representation in numerical weather prediction (NWP) and climate models remains a formidable challenge (e.g. Rodwell et al., 2013; Willison et al., 2013). In particular, the intensification of extratropical cyclones was found to be highly sensitive to the adequate representation of diabatic processes (Kuo et al., 1991; Fink et al., 2012). The present study aims at advancing the understanding of the relative importance of individual diabatic processes during the intensification period of extratropical cyclones.

75 In order to go beyond single case studies, a relatively large set of 288 extratropical cyclones from a series of twelve 35-day model simulations is investigated in this paper. The relevance of diabatic processes is assessed by tracing PV tendencies along backward trajectories following the approach introduced by Crezee et al. (2017) and refined by Spreitzer et al. (2019). This enables the assessment of the relative contribution of different diabatic processes to the modification of PV in a large set of extratropical cyclones and to investigate the variability of relevant processes across different cases.


80 2 Data and methods

The model simulations together with the physical tendencies considered in this study are described in Sect. 2.1. Based on temperature and momentum tendencies of each parametrized process, hourly PV tendencies are computed and accumulated along backward trajectories in Sect. 2.2. Finally, Sect. 2.3 introduces the cyclone and front tracking used to identify low-level PV anomalies within frontal regions. Following this approach, the contribution of different diabatic processes to PV anomalies
 85 along the frontal features of extratropical cyclones can be quantified.

2.1 Model simulations

This investigation is based on simulations with the Integrated Forecasting System (IFS) model of the European Centre for Medium-Range Weather Forecasts (ECMWF). The IFS version 43R1, which was operational at ECMWF between November 2016 and July 2017, is run at a cubic-octahedral spectral truncation of TCo639 and with 137 vertical layers. The horizontal
 90 resolution corresponds to roughly 16 km, and fields are interpolated to a regular grid of 0.4° (approximately 30 km at 45°). Besides standard meteorological fields, the temperature and momentum tendencies associated with each subgrid-scale physical processes implemented in the model are additionally archived as described by Spreitzer et al. (2019) and Attinger et al. (2019).



Table 1. Abbreviations and description of the diabatic processes considered in this study 

| Abbreviation | Process | Physical tendency |
|---------------------------------|--|-----------------------|
| APV_{tot} | Sum of all physical processes | $Q_{tot} + F_{tot}$ |
| APV_{ls} | Large-scale microphysics | Q_{ls} |
| APV_{rad} | Long-wave and short-wave radiation | Q_{rad} |
| $APV_{conv_t} + APV_{conv_m}$ | Convection | $Q_{conv} + F_{conv}$ |
| $APV_{turb_t} + APV_{turb_m}$ | Turbulence and gravity wave drag (non- and orographic) | $Q_{turb} + F_{turb}$ |
| APV_{cond} | Condensation of water vapor | Q_{cond} |
| APV_{evc} | Evaporation of cloud water | Q_{evc} |
| APV_{evr} | Evaporation of rain | Q_{evr} |
| APV_{dep} | Depositional growth of ice | Q_{dep} |
| APV_{melts} | Melting of snow | Q_{melts} |
| APV_{melti} | Melting of ice | Q_{melti} |
| APV_{subs} | Sublimation of snow | Q_{subs} |
| APV_{subi} | Sublimation of ice | Q_{subi} |
| APV_{frz} | Freezing of cloud droplets | Q_{frz} |
| APV_{rime} | Riming of cloud droplets | Q_{rime} |
| APV_{lwh} | Long-wave radiation (heating) | Q_{lwh} |
| APV_{lwc} | Long-wave radiation (cooling) | Q_{lwc} |
| APV_{sw} | Short-wave radiation | Q_{sw} |

We refer to these studies for additional information about the parametrization schemes used in the IFS model. An overview of the physical processes considered in this study is given in Table 1. Note that temperature tendencies of each process represented by the cloud microphysics parametrization are available, whereas for the convection scheme, only the sum of all phase changing processes described therein are retrieved.

For the purpose of assessing the dynamical influence of diabatic processes in a large number of extratropical cyclones, a series of free simulations has been performed. ECMWF analysis fields from the first day of each month from December 2017 until November 2018 are used as initial conditions for twelve 35-day simulations. We don't refer to these simulations as forecasts, as they of course strongly deviate from reality after a few days. However, the simulated cyclones can be considered as physically consistent and in this sense "realistic", even if they do not correspond to the observed weather in this one-year period.



2.2 Linking diabatic processes to PV modification

The PV framework is adopted to assess the relevance of diabatic processes. Following Ertel (1942), the modification of PV
 105 along the flow by tendencies of potential temperature (Q_i) and momentum (\mathbf{F}_i) can be written as

$$\text{PVR}_i = \frac{1}{\rho} (\boldsymbol{\eta} \cdot \nabla Q_i + \nabla \times \mathbf{F}_i \cdot \nabla \theta), \quad (1)$$

where PVR describes the material rate of change in PV, ρ the air density, $\boldsymbol{\eta}$ the absolute vorticity vector, θ the potential
 temperature, and subscript i the considered process. Using hourly 3D temperature and momentum tendencies from the IFS
 simulations, Eq. (1) can be used to diagnose the modification of PV due to each physical process shown in Table 1. Note that
 110 the IFS only imposes horizontal momentum tendencies. Therefore, the second term on the right hand side of Eq. (1) can be
 decomposed into a PV generation term associated with the horizontal gradient of potential temperature and another associated
 with the vertical gradient of potential temperature

$$\frac{1}{\rho} (\nabla \times \mathbf{F}_i \cdot \nabla \theta) \approx \frac{1}{\rho} \left\{ -\frac{\partial \dot{v}}{\partial z} \cdot \frac{\partial \theta}{\partial x} + \frac{\partial \dot{u}}{\partial z} \cdot \frac{\partial \theta}{\partial y} + \left(\frac{\partial \dot{v}}{\partial x} - \frac{\partial \dot{u}}{\partial y} \right) \cdot \frac{\partial \theta}{\partial z} \right\}. \quad (2)$$

Instantaneous diabatic PV rates can be noisy and might not be directly insightful to understand the formation of large-
 115 amplitude PV anomalies. Therefore, it is necessary to consider the temporal evolution of PV along air parcel trajectories
 (Crezee et al., 2017). Similar to Spreitzer et al. (2019), the change in PV at the location $\mathbf{x}(t_0)$ due to process i can be described
 by integrating PVR_i over the backward trajectory $\mathbf{x}(t)$ from time t to t_0

$$\text{APV}_i(\mathbf{x}(t_0), t) = \int_t^{t_0} \text{PVR}_i(\mathbf{x}(\tau), \tau) d\tau, \quad (3)$$

where APV is the accumulated PV tendency and t_0 is the start time of the trajectory. Since only hourly values of PVR_i are
 120 available from the model, Eq. (3) is approximated by summing the hourly PVR fields along the trajectory

$$\text{APV}_i(\mathbf{x}(t_0), t) \approx \sum_{k=0}^{n-1} \text{PVR}_i(\mathbf{x}(t_k), t_k) \Delta t, \quad (4)$$

where n (in hours) is the relevant timescale of PV modification. Based on the results from cyclones in one winter and one
 summer month, we found that low-level diabatic PV modification generally occurs on timescales of less than 15 hours (see
 Attinger, 2020). Therefore, in this study we adopt a trajectory integration period of 15 hours, which is slightly shorter compared
 125 to previous studies that used an integration period of 24 hours (e.g. Crezee et al., 2017; Attinger et al., 2019). Note that the final
 time step (t_n) of the backward trajectory is not included in the summation since the hourly PVR tendencies are representative



for the previous hour. Finally, the total change of PV along the flow can be described by the sum of individual APV terms from the large-scale microphysics, radiation, convection, and turbulence schemes


$$\Delta PV = APV_{ls} + APV_{rad} + APV_{conv_t} + APV_{conv_m} + APV_{turb_t} + APV_{turb_m} - RES, \quad (5)$$

130 where RES is the residual. A number of factors can contribute to the residual, including the non-conservation of PV by the dynamical core (Saffin et al., 2016), the high temporal variability of the considered processes (Neiman and Shapiro, 1993) that are not fully captured by our hourly output fields, interpolation errors during the trajectory and PV computation, or missing PV source terms (Lackmann and Yablonsky, 2004). We refer to Spreitzer et al. (2019) and Attinger et al. (2019) for an in-depth discussion of the potential causes leading to the residual.

135 Backward trajectories are integrated for 15 h using the Lagrangian analysis tool LAGRANTO (Wernli and Davies, 1997; Sprenger and Wernli, 2015). Trajectories are started hourly from each grid point in the Northern Hemisphere and on each model level. PVR due to individual processes are then interpolated to and accumulated along the trajectories following Eq. (4).

2.3 Identification of cyclones and fronts

Extratropical cyclones and their accompanying fronts are automatically identified using a customized cyclone and front tracking
 140 framework. Cyclones are identified by searching for local minima in the sea-level pressure (SLP) field (< 1000 hPa) or local maxima in the relative vorticity field on 850 hPa ($> 1.4 \times 10^{-4} s^{-1}$). The extent of cyclones is defined by the largest enclosing SLP contour that contains no secondary SLP minimum. The selection of the outermost closed contour is limited by three criteria: (i) its SLP value must be below 1015 hPa, (ii) its SLP value must not exceed the cyclone's core value by more than 40 hPa, and (iii) the enclosed area must be smaller than $44'000$ km multiplied by the latitude of the cyclone center. Areas of
 145 low SLP in mountainous areas are removed to avoid spurious signals. Cyclones are then tracked in time and only retained if they reach a lifetime of more than 24 h.

 approach identifies approximately 100 extratropical cyclones in the Northern Hemisphere during each 35-day simulation period. As diabatic processes play an important role for the intensification of extratropical cyclones (e.g. Ahmadi-Givi, 2002), only the most rapidly intensifying cyclones are selected in this study. As a measure for their intensification, the normal-
 150 ized central pressure deepening rate (NDR) according to Sanders and Gyakum (1980) is computed for each cyclone

$$NDR = \frac{\Delta SLP}{24} \cdot \frac{\sin(60^\circ)}{|\sin(\phi)|}, \quad (6)$$

where ΔSLP is the central pressure difference along the track evaluated over 24 h, and ϕ the mean latitude of the cyclone during this period. Extratropical cyclones that reach a value of $NDR \geq 1$ are defined as explosive cyclones (Sanders and Gyakum, 1980). Only the most strongly deepening systems are retained for our analysis (see Sect. 3.1).

155 Extending upon the work from Parfitt et al. (2017), fronts are identified based on a combination of criteria that rely on relative vorticity (ζ), equivalent potential temperature (θ_e), and the horizontal wind (v), averaged between 950 and 850 hPa. Three frontal measures are used to identify frontal zones:



M_1 The horizontal gradient of equivalent potential temperature ($\nabla_h \theta_e$) evaluated over 5 grid points (corresponding to approximately 220 km at 45°N).

160 M_2 The horizontal advection of equivalent potential temperature ($v \nabla_h \theta_e$).

M_3 The average relative vorticity (ζ) evaluated over 9 neighboring grid-points.

The thresholds given in Table 2 correspond to the combination that best identified manually diagnosed fronts of the most rapidly intensifying cyclones from the January simulation.

Table 2. Thresholds used to identify the cold, warm, and bent-back fronts, respectively

| Feature | M_1 (K/2°) | M_2 (K m s ⁻¹) | M_3 ($\times 10^{-4}$ s ⁻¹) |
|-----------------|--------------|------------------------------|--|
| Cold front | ≥ 5.9 | ≥ 32.3 | ≥ 0.1 |
| Warm front | — | ≤ -195 | — |
| Warm front | ≥ 4.1 | ≤ -43 | ≥ 0.1 |
| Bent-back front | — | — | ≥ 3 |
| Bent-back front | ≤ 5 | — | ≥ 1.9 |

Finally, a circular region with a radius of 5 grid points (2°) defines the cyclone center. Attinger (2020) discusses in more detail
 165 the mathematical derivation of the frontal measures as well as the automatic approach used to select the thresholds.

We focus on regions of anomalously high (≥ 1 PVU) and low (≤ -0.1 PVU) PV, subsequently referred to as positive and negative PV anomalies, that occur along the cold and warm fronts. As the bent-back front is generally located close to the cyclone center and since this region is primarily associated with high PV, we combine these two features to form another region of interest. This approach defines five mutually exclusive categories of PV anomalies in each cyclone: positive and negative
 170 PV anomalies along the warm and cold fronts, respectively and positive PV anomalies in the cyclone center, including the bent-back front (see contours in Fig. 2b).

3 Results

3.1 Selection of cyclones

A variety of different extratropical cyclones occur in each 35-day IFS simulation. The total number of extratropical cyclones
 175 identified in the Northern Hemisphere in each month, together with the amount of explosively deepening cyclones is provided in the upper part of Table 3. A larger number of extratropical cyclones, which are also more often rapidly intensifying, are identified during winter than in summer. Additionally, fewer rapidly intensifying extratropical cyclones occur in summer than during winter. Taking the variability in cyclone intensification into account, an extended warm and cold seas are defined.



Months with (in total) more than 9 explosively deepening cyclones are assigned to the cold season (October to March) whereas
 180 the other months are assigned to the warm season (April to September).

Table 3. Number and intensity of extratropical cyclones in the Northern Hemisphere identified in each simulation period (DEC refers to the 35-day simulation initialized on 1 December 2017). The upper part shows the total number of identified extratropical cyclones and how many of them are explosively deepening. The lower part shows how many of the 24 selected extratropical cyclones are explosively deepening and their average normalized central pressure deepening rate.

| | DEC | JAN | FEB | MAR | APR | MAY | JUN | JUL | AUG | SEP | OCT | NOV |
|-------------------------------------|------|------|------|------|------|-----|------|------|------|------|------|------|
| Total extratropical cyclones | 118 | 124 | 103 | 127 | 96 | 103 | 91 | 95 | 120 | 103 | 109 | 117 |
| Total explosively deepening | 20 | 24 | 17 | 10 | 8 | 4 | 2 | 1 | 1 | 7 | 15 | 14 |
| Selected cyclones with $NDR \geq 1$ | 19 | 18 | 14 | 9 | 8 | 4 | 1 | 0 | 1 | 2 | 13 | 12 |
| Average NDR of selected cyclones | 1.37 | 1.58 | 1.17 | 0.93 | 0.91 | 0.7 | 0.42 | 0.42 | 0.48 | 0.58 | 1.12 | 1.09 |

In order to ensure a consistent data set for the subsequent analysis, manual removal of a number of cyclones is required. Specifically, we remove extratropical transition events of tropical cyclones, extratropical cyclones that lack a pronounced low-level PV signature, cyclones accompanied by intense secondary systems along their cold front (as this makes the automatic front affiliation difficult), and cyclones whose fronts cannot be identified with sufficient accuracy. Based on this homogenized
 185 data set, 24 cyclones are selected from each simulation, resulting in 144 systems per season. Note that we choose 24 as the number of investigated systems in each month, as this is the largest number of explosively deepening cyclones observed in a single month. However, we do not require the selected cyclones to exceed 1 NDR because only a few systems would satisfy this criterion. Instead we pick the 24 most rapidly intensifying cyclones after removal of unsuitable candidates as described above. Thereby, we sample an equal number of intense cyclones in each month, which allows us to compare results from different
 190 seasons. The number of rapidly intensifying cyclones and the average NDR of the 24 selected cyclones in each month is shown in the lower part of Table 3.

Figure 1 shows the geographical distribution of the selected cyclones. During the cold season, the selected cyclones are almost exclusively oceanic and located in the North Atlantic and North Pacific storm tracks (Fig. 1a). One Mediterranean, two subtropical, and one continental cyclone are also included in the evaluation. In the warm season, fewer of the selected
 195 systems occur along the storm tracks, especially over the North Pacific, and more continental cyclones are considered (Fig. 1b). Good qualitative agreement is found with the cyclone climatology based on ERA-40 reanalysis (Wernli and Schwierz, 2006), although absolute frequencies are lower due to the constrained sample size in this study.

During the cold season, a larger fraction of the selected cyclones are accompanied by a bent-back front (77) compared to the warm season (60). The number of cold fronts is similar in the cold and warm seasons (119 and 117, respectively), and 144 warm
 200 fronts are found in both seasons. Recall that cyclones that do not feature clearly identifiable fronts were manually removed.

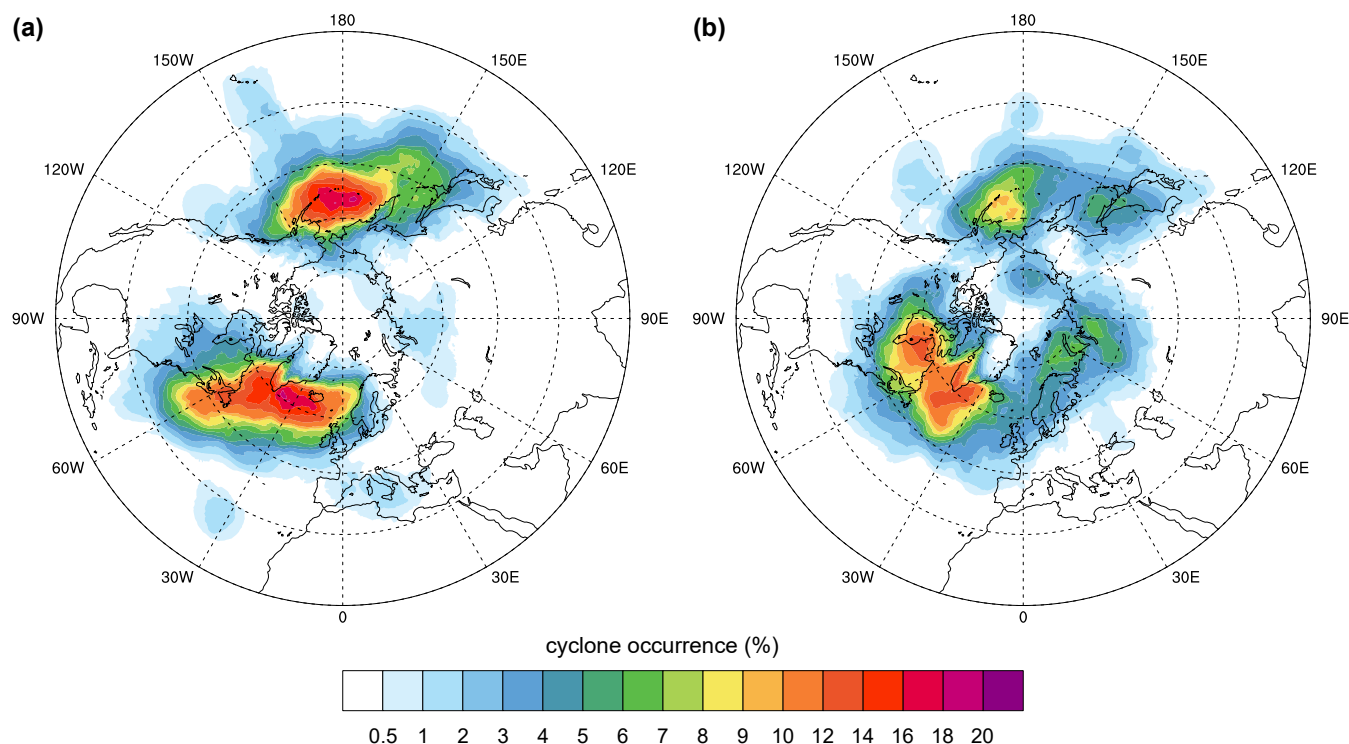


Figure 1. Geographical distribution of extratropical cyclones considered in this study. For (a) the cold season and (b) the warm season. Percentages depict the fraction of time steps with a cyclone present, i.e. 10% corresponds to roughly 21 days.

3.2 Investigated PV anomalies

Table 4 provides an overview of the average intensity (PVU), size (km^2), and height (hPa) of the five categories of low-level PV anomalies per season investigated in this paper. Values are obtained from the 144 selected extratropical cyclones in each season and averaged over the 24 h period with maximum cyclone intensification. In both seasons, positive PV anomalies are generally at a higher altitude and have a larger extent than their negative counterparts. In the warm season, both negative and positive PV anomalies are more intense than during the cold season. The warm front is characteristic of the largest positive and the smallest negative PV anomalies.

The different low-level PV anomalies vertically averaged between 840 and 740 hPa are exemplarily shown in Fig. 2a for a single cyclone. Positive PV anomalies (solid contours) occur along the fronts and in the cyclone center, whereas negative PV anomalies (dashed contours) are found to the west of the cold front. Note that negative PV anomalies along the warm front generally occur at a lower altitude. The net PV change along 15 h backward trajectories (Fig. 2b) is similar to the full PV (Fig. 2a), indicating that a substantial part of the PV anomalies is produced within the last 15 h. Regions of increased PV (orange shading) are observed along the fronts and in the cyclone center, whereas decreased PV (purple shading) is found south of the warm front and west of the cold front. An area of reduced PV is found south of the cyclone center although full PV



Table 4. Average intensity, area, and altitude of investigated PV anomalies.

| | | cold front | | warm front | | cyclone center |
|-------------|-------------------------|-------------------------|----------------------------|-------------------------|----------------------------|-------------------------|
| | | $PV \geq 1 \text{ PVU}$ | $PV \leq -0.1 \text{ PVU}$ | $PV \geq 1 \text{ PVU}$ | $PV \leq -0.1 \text{ PVU}$ | $PV \geq 1 \text{ PVU}$ |
| cold season | PV (PVU) | 1.54 | -0.34 | 1.52 | -0.34 | 1.86 |
| | Area (km ²) | 1'117'629 | 429'089 | 1'950'320 | 88'262 | 996'628 |
| | Altitude (hPa) | 837.5 | 983.1 | 839.9 | 961.4 | 832.5 |
| warm season | PV (PVU) | 1.68 | -0.38 | 1.72 | -0.38 | 2 |
| | Area (km ²) | 1'282'178 | 311'692 | 2'193'129 | 69'739 | 839'990 |
| | Altitude (hPa) | 847.2 | 975.0 | 868.2 | 963.8 | 843.7 |

remains positive. However, this area is not further considered as it does not fulfill our criterion of a PV anomaly. Additionally, an area of high-PV occurs north of the warm front (Fig. 2a) which does not coincide with a region of strong PV increase (Fig. 2b). In this region, high-PV air masses are thus primarily advected

For the assessment of the physical processes that modify PV, positive and negative PV anomalies are identified at the fronts and in the center of the cyclone. The identified anomalies along the cold front, warm front, and central region are highlighted by blue, red, and dark gray contours, respectively (Fig. 2b,c,d). Total APV (i.e. Eq. (4) evaluated for all processes) is shown in Fig. 2c. Ideally, this should correspond to the net PV change along the trajectories (Fig. 2b), assuming complete information on the temperature and momentum tendencies from each parametrized process, perfect trajectories, and full PV conservation by the model's advection scheme. Generally, good agreement between total APV and the net PV change is found. Main discrepancies are observed south of the cyclone center, where pronounced negative total APV is diagnosed. Finally, the contribution of condensation to the modification of PV along trajectories is shown in Fig. 2d. As expected, condensation is responsible for a large fraction of the PV increase along the fronts and in the cyclone center. Additionally, negative APV due to condensation occurs west of the cold front and east of the bent-back front.

3.3 Systematic assessment of diabatic PV modification in extratropical cyclones

Focusing on the five areas of anomalous PV introduced above, we systematically assess the physical processes that modify PV in the most rapidly intensifying extratropical cyclones. Positive PV anomalies between the surface and 550 hPa and negative PV anomalies between the surface and 850 hPa are considered. These levels have been selected to take into account the majority of grid points that exceed the PV anomaly threshold used (not shown). Beginning with the cold season, the 24 h period of strongest cyclone deepening is identified and the area-averaged APV of each process is calculated at every hour for each PV anomaly. When averaging hourly contributions over all 144 cyclones, the mean temporal evolution of the processes that contribute to any PV anomaly can be calculated.

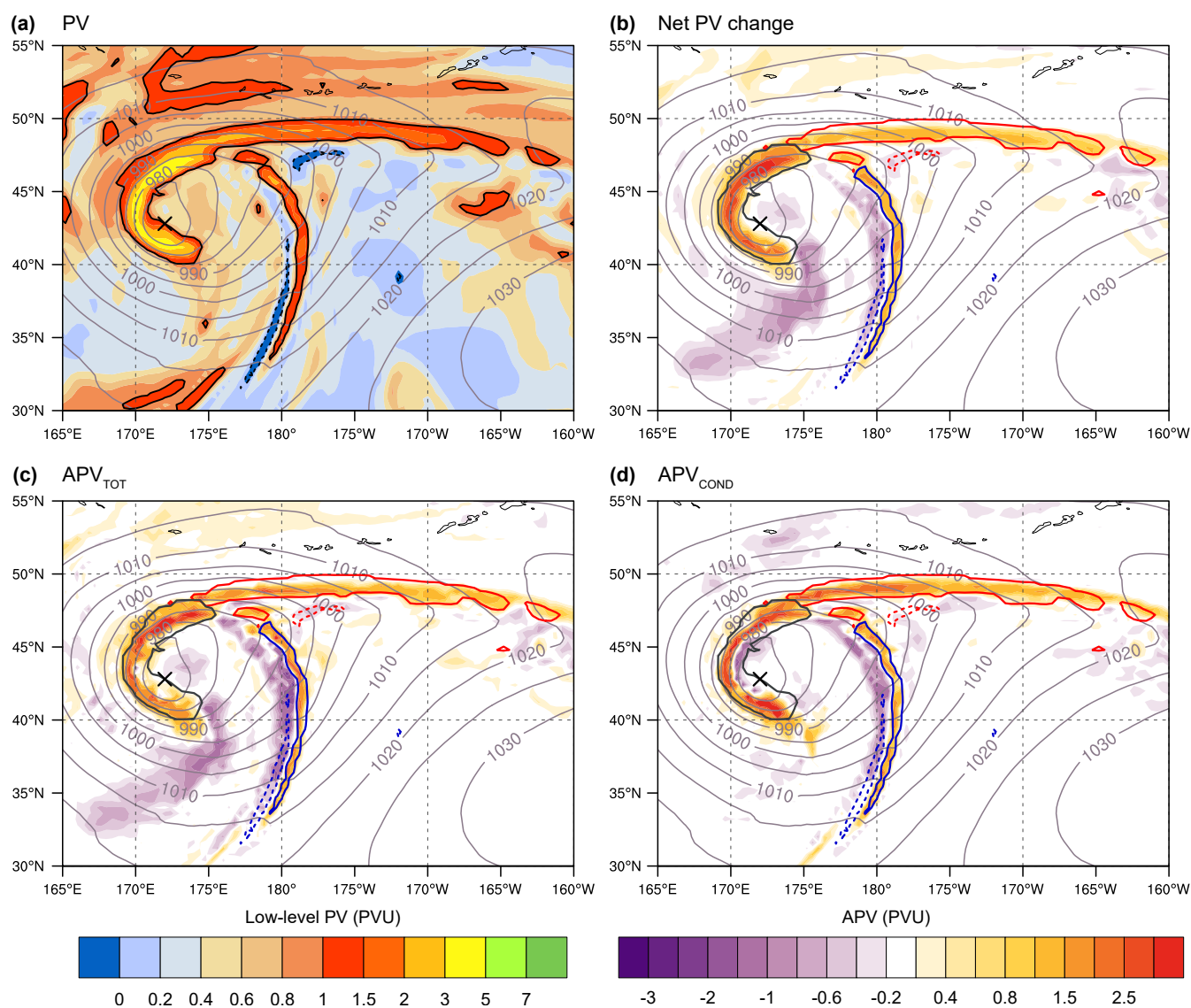


Figure 2. An extratropical cyclone over the North Pacific at the time of maximum intensification. (a) Vertically averaged PV between 840 hPa and 780 hPa. Regions with $PV \geq 1$ PVU and $PV \leq -0.1$ PVU are highlighted by solid and dashed black lines, respectively. (b) Net PV change, (c) total diagnosed PV modification, and (d) effect of condensation on PV along 15-h backward trajectories. The positive and negative PV anomalies along the cold front (blue solid and dashed lines), the positive and negative PV anomalies along the warm front (red solid and dashed lines), and the positive PV anomaly in the cyclone center (dark gray solid line) are highlighted. The sea level pressure (SLP) minimum is marked by the cross. The sea level pressure (SLP) minimum is marked by the cross. The sea level pressure (SLP) minimum is marked by the cross.



Figure 3a shows the average contribution of different processes to the positive PV anomaly in the cyclone center. Each line represents the average PV tendency of different processes accumulated over 15 h backward trajectories ending in the positive PV anomaly of the cyclone center between the surface and 550 hPa. On average, this region is associated with roughly 250'000 trajectories (about 2'000 per cyclone) at each time step (dotted line). The number of trajectories increases steadily during cyclone intensification whereas the mean absolute PV (dark blue) remains mostly constant. Thus, the region with a positive PV anomaly grows during cyclone deepening which is indicative of an increase in the cyclonic circulation and hence intensity of the systems. Total APV (black) is primarily comprised of condensation (red), turbulent momentum tendencies (green dashed), and convection (orange solid). Additionally, minor positive APV from snow melting is observed towards the end of the intensification period (cyan).

Positive contribution is partially offset by negative APV due to turbulent temperature tendencies (green). Since turbulence dilutes heating or cooling tendencies, this process is generally expected to produce APV tendencies of opposite sign to the leading diabatic APV tendency. The intensity of negative APV generated by turbulent temperature tendencies increases during the deepening of the cyclones, in line with the slight increase in positive contributions from condensation, turbulent momentum tendencies, and convection. Finally, weak negative APV tendencies by long-wave radiative heating occur.

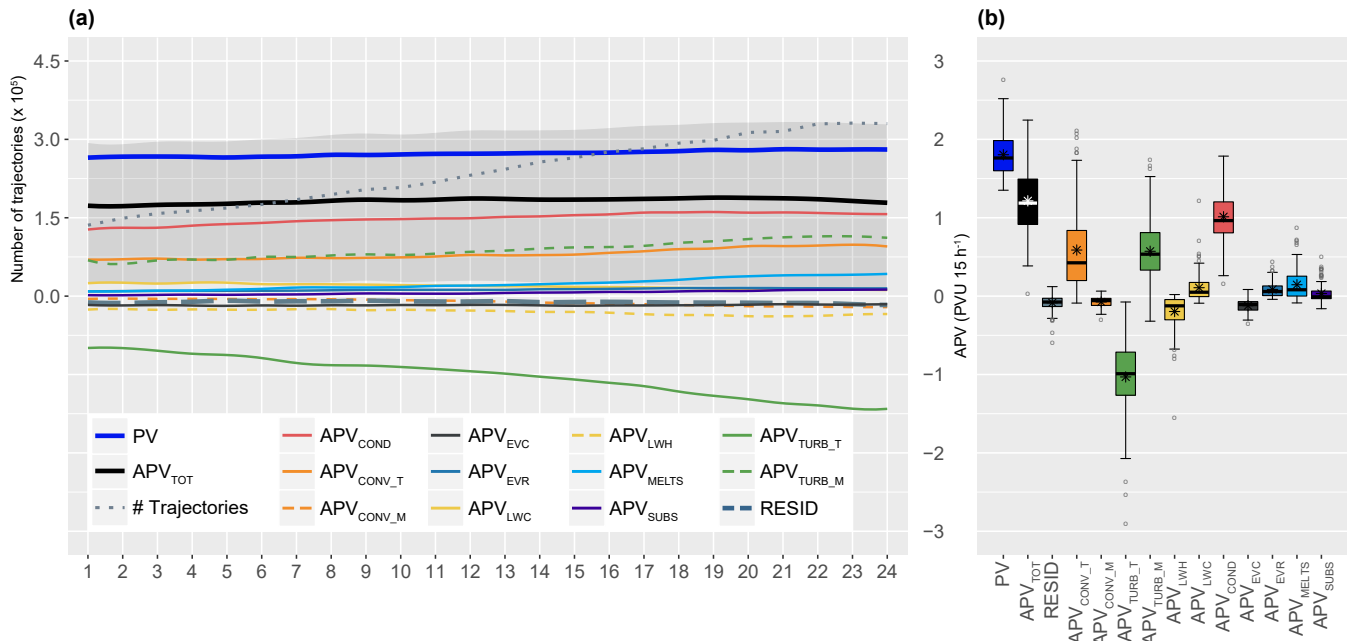


Figure 3. Physical processes that contribute to the positive PV anomaly ($PV \geq 1$ PVU) in the cyclone center between the surface and 550 hPa during the 24 h period of strongest cyclone intensification. (a) Time series of APV averaged over the 144 cyclones in the cold season and (b) distribution of APV tendencies across all cyclones. The interquartile range is shown by the boxes, the whiskers extend 1.5 times the interquartile range, the median is shown by the bold horizontal line, the mean by the star, and outliers are shown as open circles.



250 Figure 3a reveals that contributions from different physical processes to the positive PV anomaly in the cyclone center are temporally largely consistent when averaging over 144 cyclones. Similarly consistent results are found for the positive and negative PV anomalies along the warm and cold fronts (not shown). However, when considering individual cyclones separately, a large variability in the contribution of the most relevant processes (condensation, turbulent exchange of momentum, and convection) is found (Fig. 3b). In some cyclones, condensation only contributes insignificantly, while larger APV tendencies
 255 from other processes such as melting or sublimation of snow are observed.

To take this large case-to-case variability into account, we rank the area-weighted mean contributions from different processes to individual PV anomalies. This yields information on the fraction of cyclones that share the same process as the most dominant for the generation of the considered PV anomaly. Similarly, we can identify the most relevant opposing process, i.e. the process that produces PV with the opposite sign of the anomaly. Since we found little temporal variability during the
 260 24 h period of most rapid intensification (Fig. 3a), ranked contributions are averaged over this entire period. Note that for this assessment, trajectories are only used if (i) they have a residuum smaller than 50% of the total diagnosed PV modification and (ii) the diagnosed PV change has the same sign as the actual change in PV.

For the positive PV anomaly along the cold front (Fig. 4a, first panel), condensation is the most important process in 53% of all cyclones with an area-weighted mean APV of 0.88 PVU. Convection is more relevant than condensation in 29% of all
 265 cyclones, contributing 1.17 PVU on average. 14% of the cyclones occur in a particular environment promoting intense long-wave radiative cooling, which contributes 0.52 PVU to the positive PV anomaly along the cold front. These cyclones likely do not experience strong cloud formation as the APV value associated with long-wave radiative cooling is markedly lower than the mean contribution from condensation and convection. Additionally, in about 5%, other processes are the most relevant for the generation of PV along the cold front. Turbulent temperature tendencies are the most dominant opposing process in 82%
 270 of all cyclones, reducing PV on average by -0.46 PVU (not shown).

Condensation is again the most dominant process for the generation of the positive PV anomaly along the warm front (Fig. 4a, second panel), increasing PV on average by 0.86 PVU in every second cyclone. Turbulent momentum tendencies are responsible for the production of 0.98 PVU in 38% of all cases. Comparatively few cyclones (10%) are found where convection
 is the most relevant process, increasing PV by 0.94 PVU. Negative APV of -0.38 PVU due to turbulent temperature tendencies
 275 are again found in a large number of cyclones (60%). Additionally, about every third cyclone is characterized by -0.45 PVU due to long-wave radiative heating (not shown).

In the cyclone center and along the bent-back front (Fig. 4a, third panel), PV is primarily produced by condensation (1.27 PVU in 71%), followed by convection (1.37 PVU in 16%), and turbulent momentum tendencies (1.28 PVU in 12%), consistent with Fig. 3a. Turbulent temperature tendencies strongly offset the PV budget (-0.91 PVU) in almost all cases (not
 280 shown).

The negative PV anomaly along the cold front is mainly influenced by boundary layer processes (Fig. 4b, first panel). Turbulent momentum tendencies and long-wave radiative heating are the primary processes reducing PV by -1.49 PVU and -1.9 PVU in 46% and 39% of all cyclones, respectively. In addition, turbulent temperature tendencies reduce PV on average by -1.47 PVU in 14% of all cyclones. Considering the most relevant opposing processes, long-wave radiative cooling and

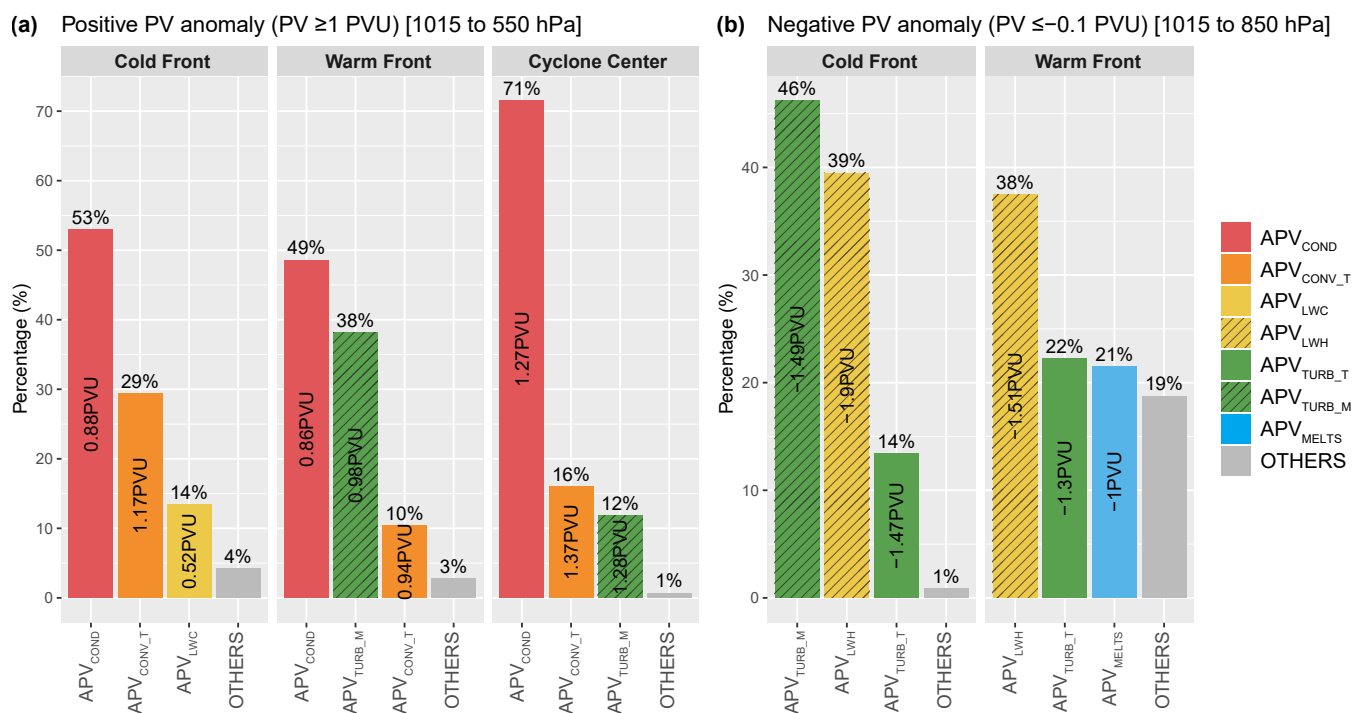


Figure 4. Prevalence of the dominant processes for the generation of (a) the positive PV anomaly ($PV \geq 1$ PVU) between the surface and 550 hPa and (b) the negative PV anomaly ($PV \leq -0.1$ PVU) between the surface and 850 hPa during the cold season. Ranks are computed from the area-weighted mean APV of each process averaged over the entire 24 h period of most rapid cyclone intensification. Percentages indicate the fraction of cyclones with a specific process as the most important one and numbers show the area-weighted mean APV averaged over all cyclones.

285 turbulent temperature tendencies produce about 1.14 PVU and 1.47 PVU in 46% and 34% of all cyclones, respectively (not shown).

Compared to the cold front, decidedly different processes reduce PV along the warm front (Fig. 4b, second panel). In 38% of all cases, long-wave radiative heating dominates and is responsible for a reduction by -1.51 PVU. In 22% and 21%, turbulent temperature tendencies and melting of snow generate -1.3 PVU and -1 PVU, respectively. Additionally, various other processes are responsible for the negative PV anomaly in every fifth cyclone, indicating the large variability in relevant processes. Negative PV tendencies are offset by turbulent temperature tendencies (1.16 PVU in 47%) and long-wave radiative cooling (0.57 PVU in 24%, not shown).

The same processes as described for the cold season are responsible for the generation of positive PV anomalies during the warm season (Fig. 5a). However, the fraction of cyclones with convection as the most relevant process strongly decreases. Specifically, long-wave radiative cooling becomes more prevalent (20%) than convection (9%) in generating positive PV anomalies at the cold front, while condensation remains the primary PV producer (55%). Surprisingly, turbulent momentum tendencies (54%) become more important than condensation (39%) and convection (3%) along the warm front. Finally,

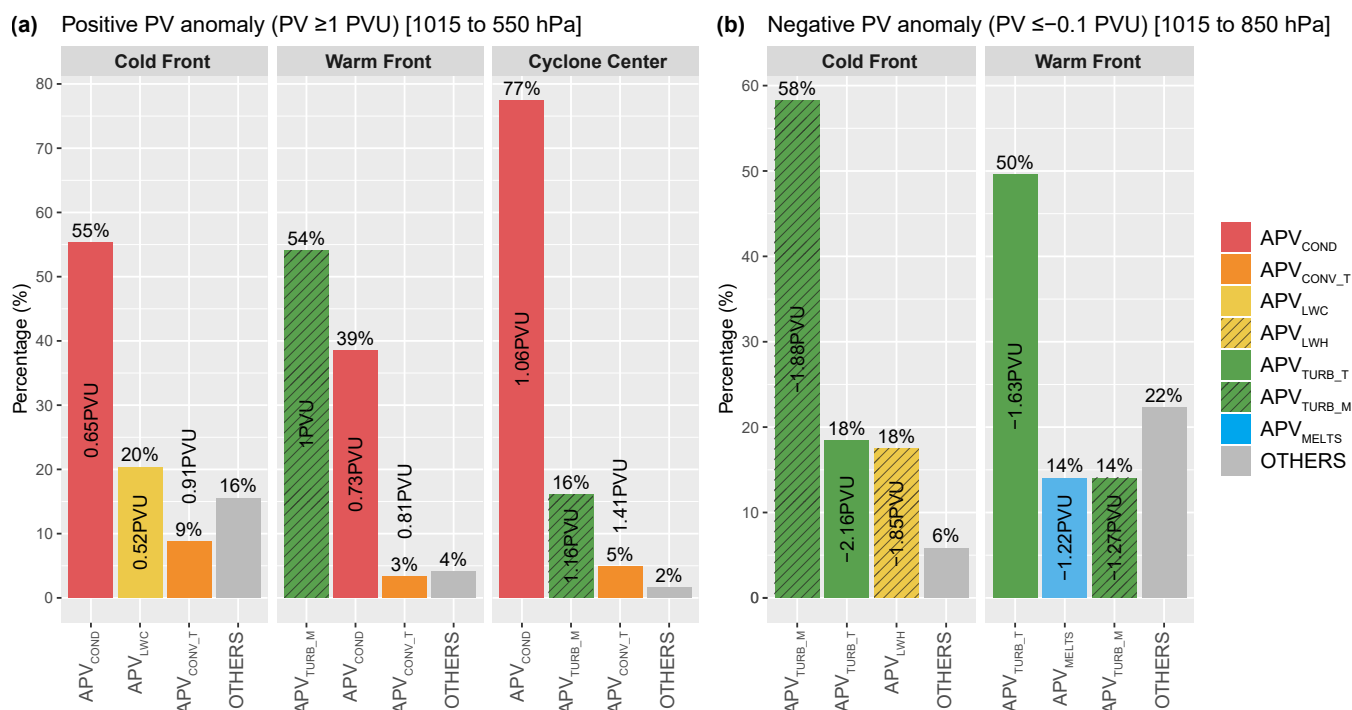


Figure 5. As Fig. 4, but for the 144 cyclones in the warm season.

fewer cyclones experience strong PV production due to convection (5%) than turbulent momentum tendencies (16%) in the center, while condensation remains the dominant process (77%).

300 The processes that generate negative PV anomalies in extratropical cyclones during the warm season are shown in Fig. 5b. Along the cold front, negative PV is primarily generated by turbulent momentum tendencies (58%), followed by turbulent temperature (18%), and long-wave radiative heating (18%). Along the warm front, the relevance of long-wave radiative heating found in the cold season (Fig. 4b, second panel) diminishes during the warm season with negative PV being produced by turbulent temperature (50%), melting of snow (14%), and turbulent momentum tendencies (14%).

305 When comparing the processes that generate positive PV anomalies across the three studied regions in the cold season, we find that the same process dominates along the warm front and in the cyclone center in approximately 28% of all cyclones (not shown). Moreover, the same process dominates in three regions in 25% of all cases, whereas in roughly one third of all cyclones, a different process generates PV in each feature. Cyclones with the same dominating process at the cold front and center, but a different one along the warm front, only account for 16% of all cyclones. Finally, a mere 4% of all cyclones are

310 characterized by the same dominating process along the warm and cold front but a different one in the cyclone center.

In 80% of all cyclones, a different process generates the negative PV anomaly along the warm and cold front. Note that since we do not investigate negative PV anomalies in the cyclone center, only two categories exist.



This section established the primary physical processes that generate pronounced PV anomalies in extratropical cyclones. Expectedly, condensation is the main driver of increased PV along the fronts. In a significant number of cyclones however, turbulent exchange of momentum along the warm front and long-wave radiative cooling at the cold front were found to be more relevant. On the other hand, no distinct physical process was found to be responsible for the generation of negative PV in general. Turbulent exchange of momentum and temperature, long-wave radiative heating, and melting of snow all significantly contribute to negative PV in a large number of systems.

3.4 The influence of the environment on the generation of positive PV anomalies

To understand the underlying mechanism driving the variability in the processes that modify PV, we examine the environment of cyclones that differ in terms of the dominant process generating PV anomalies. Specifically, we focus on the processes producing positive PV anomalies in the cold season. To this end, composites of various meteorological fields are calculated along the cold front, warm front, and cyclone center for the three main categories observed (Fig. 4a).

For the cold and warm front composites, the frontal objects need to be rotated such that they align south-north and east-west, respectively. The frontal orientation is obtained by fitting a linear regression model to the coordinates of the front. Additionally, we require higher equivalent potential temperature to the east (south) than to the west (north) of the cold (warm) front to ensure correct rotation. Frontal composites are centered on the mean frontal coordinates. Composites of the cyclone center are not rotated and simply centered on the minimum SLP.

3.4.1 The cold front

The positive PV anomaly along the cold front is primarily produced by condensation, convection, and long-wave radiative cooling during the cold season (Fig. 4a, first panel). Cold fronts whose positive PV anomaly is primarily generated by convection mainly occur over warm ocean currents, whereas those associated with long-wave radiative cooling are predominantly observed in the northern parts of ocean basins (Fig. 6a).

The environmental conditions of cold fronts whose positive PV anomaly is mainly generated by condensation are shown in the first row of Fig. 7. These fronts occur in areas of high specific humidity (Fig. 7d) and produce the most intense large-scale precipitation compared to the other categories, highlighting the relevance of cloud formation for their positive PV anomaly. Also, these cold fronts are associated with a large positive air-sea temperature difference in the warm sector (Fig. 7c). Because the surface sensible heat flux (SSHF) is proportional to the air-sea temperature difference, strong positive SSHF, i.e. a heat flux directed into the ocean, occurs just east of the cold front (Fig. 7c). This increases the stability of the boundary layer, which is in line with the low values of convective available potential temperature (CAPE) and little convective precipitation found in the vicinity of the cold front of these cyclones (Fig. 7e).

When comparing cold fronts that primarily experience PV generation by convection (Fig. 7, second row) with the former category, we find that these fronts are generally located above significantly warmer sea surface temperatures (SST, Fig. 7g). This results in a negative air-sea temperature difference covering almost the entire warm sector (Fig. 7h), leading to negative

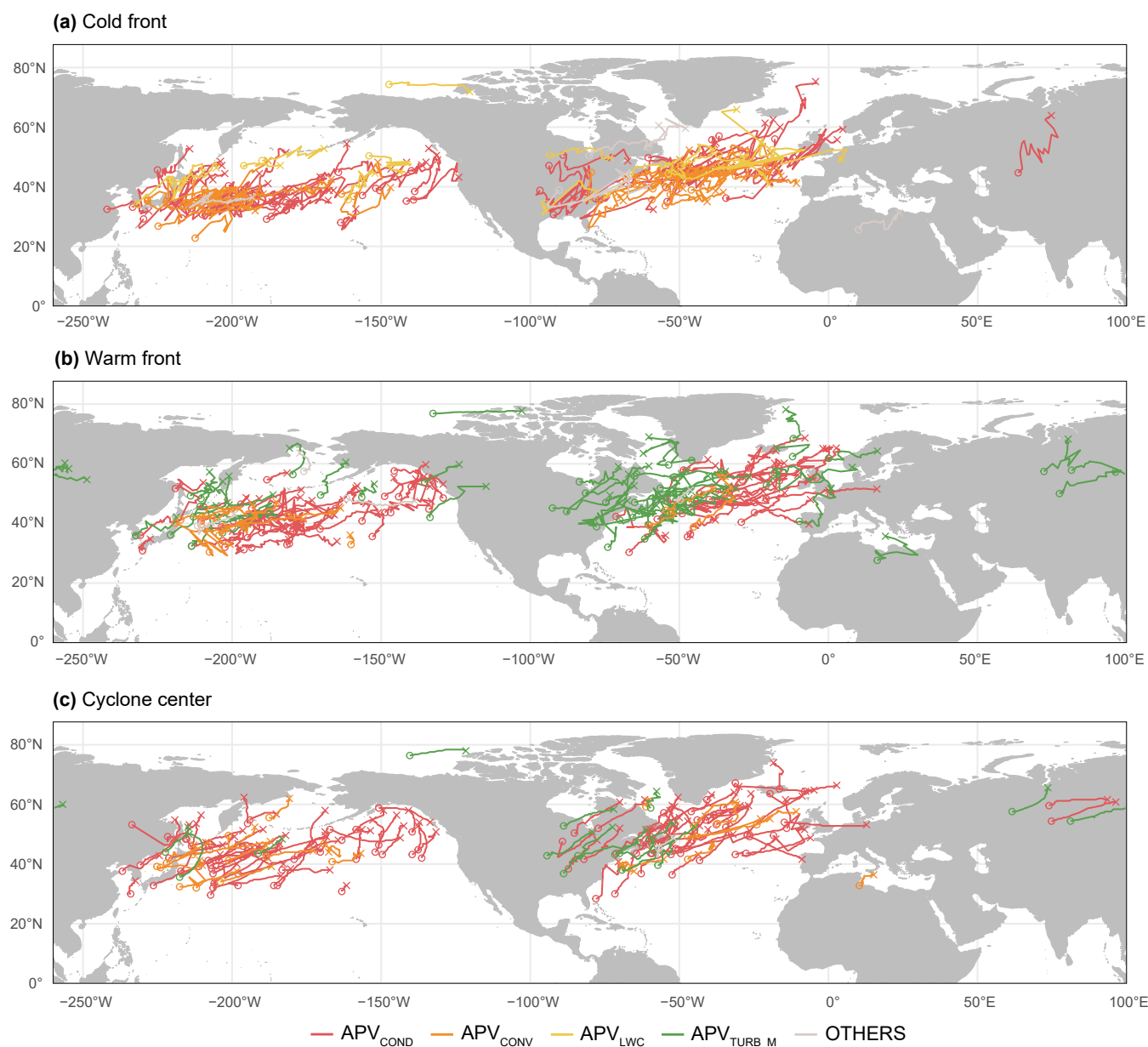


Figure 6. Geographical occurrence of (a) cold fronts, (b) warm fronts, and (c) cyclone centers for all cyclones from the cold season. Colors indicate the dominant physical process responsible for the generation of positive PV anomalies along the respective feature. Open circles indicate the beginning and crosses the end of the 24 h period of most rapid cyclone intensification.

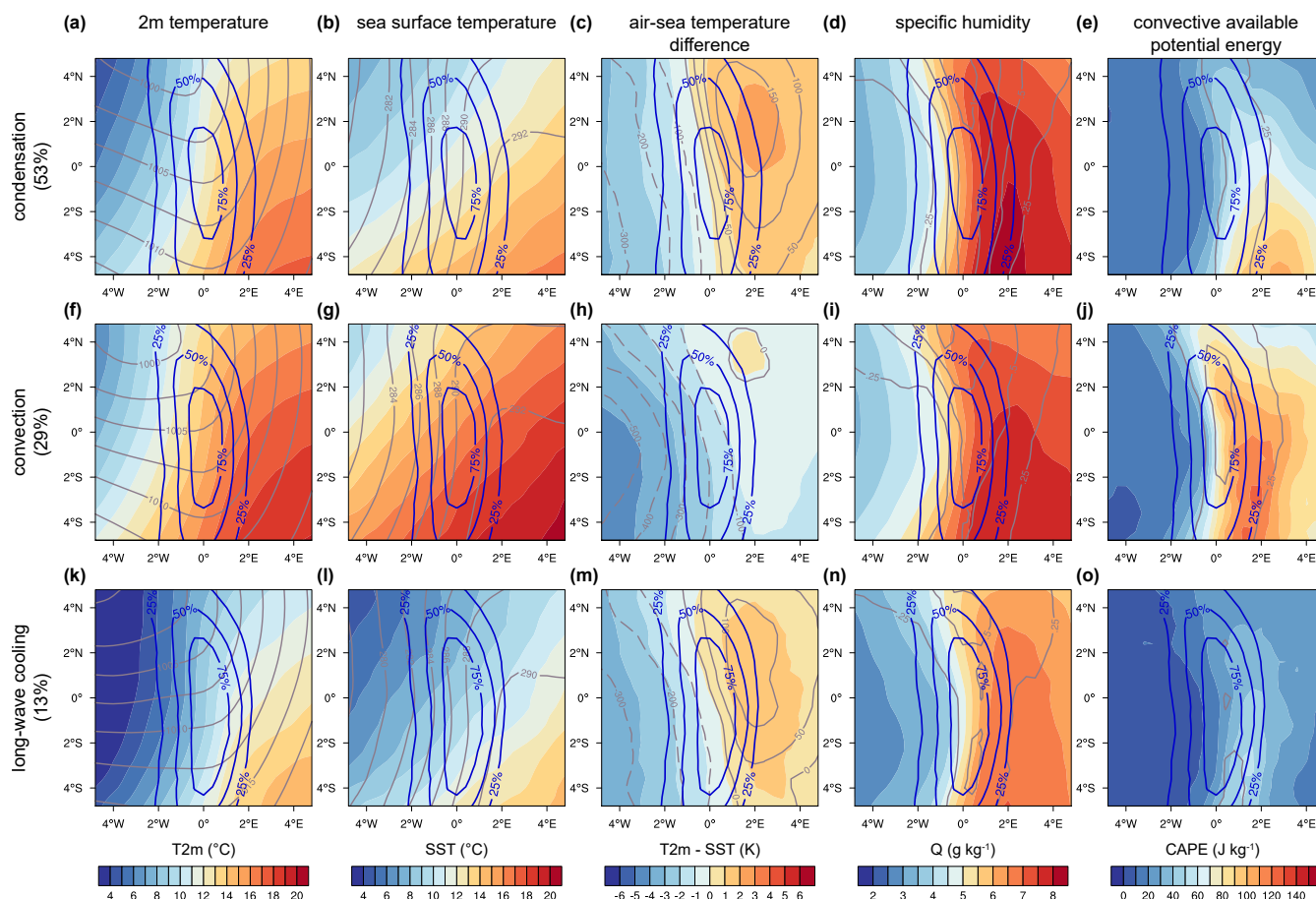


Figure 7. Composites of the environmental conditions along the cold front averaged over the 24 h period of most rapid cyclone intensification for the 144 extratropical cyclones in the cold season. Rows represent different cyclone categories based on the primary process that produces the positive PV anomaly along the cold front (Fig. 4a). Depicted are surface fields, except for specific humidity which is shown at 900 hPa. Blue contours indicate average cold front frequency while gray contours show sea level pressure (first column), θ on 900 hPa (second column), surface sensible heat flux (third column), large-scale precipitation (fourth column), and convective precipitation (last column).


SSHf east of the cold front, i.e. a heat flux directed into the atmosphere. This is likely linked to destabilization of the boundary layer and might explain why these systems are primarily associated with convection. Additionally, we find strong negative SLHF throughout the entire composite (not shown), indicating strong ocean evaporation. Note that strong negative SLHF is observed in all three categories. Intense convective precipitation and high CAPE (Fig. 7j) further emphasize the convective nature of these cyclones.

The bottom row in Fig. 7 shows the environment of cold fronts whose positive PV anomaly is mainly generated by long-wave radiative cooling. These cold fronts occur in a markedly colder environment both in terms of surface (Fig. 7k) and sea surface temperatures (Fig. 7l), further supported by the geographical distribution of these features (Fig. 6a). While the absolute values



are much lower compared to the first category, the relative air-sea temperature difference is even more pronounced (Fig. 7m). This leads to long-wave radiative cooling at the lowermost air layers in the warm sector, which is associated with intense PV production along the front (blue contours). Furthermore, because of the reduced water vapor content in colder air (Fig. 7n), less precipitation and thus condensation occurs in these cyclones. The lack of condensation together with the intense positive SSHF in the vicinity of the front explains why the positive PV anomaly along the cold front of these cyclones is primarily produced by long-wave radiative cooling.

3.4.2 The warm front


Previously, we showed that the positive PV anomaly along the warm front during the cold season is either produced by condensation, turbulent momentum tendencies, or convection (Fig. 4a, second panel). When looking at the geographical distribution of the different warm front types, we find that from  primarily associated with PV generation by convection cluster in the western part of ocean basins. Conversely, warm fronts modified by turbulent momentum tendencies are predominantly observed over land (Fig. 6b).

Warm front composites of cyclones primarily influenced by condensation are shown in the first row of Fig. 8. Similar to the cold fronts belonging into this category, we find a positive air-sea temperature difference in the warm sector (Fig. 8c). Out of the three categories, these warm fronts are associated with the largest amounts of precipitation (Fig. 8d).

The second category of warm fronts is related to the production of PV by turbulent momentum tendencies (Fig. 8, second row). These warm fronts occur in approximately 8 K colder air, which leads to reduced specific humidity and precipitation (Fig. 8i). When considering the eastward turbulent surface stress (ETSS, describing the accumulated stress on the Earth's surface by turbulence), a distinct region with negative values is found north of the warm front where the prevailing winds are easterly (Fig. 8j). Therefore, turbulence leads to eastward acceleration at the surface, which diminishes with height (i.e. $\partial u/\partial z < 0$). This occurs in a region with a strong negative meridional θ gradient ($\partial\theta/\partial y < 0$). Because these terms dominate the momentum tendency equation (second term in Eq. (2)), turbulent PV generation occurs north of the warm front.

Finally, warm fronts mainly affected by convection (Fig. 8, bottom row) are again characterized by a negative or slightly positive air-sea temperature difference in the warm sector (Fig. 8m). This leads to mainly negative SSHF in the warm sector (contours in Fig. 8m) which likely destabilizes the boundary layer and thus promotes convection. While enhanced specific humidity is found (Fig. 8n), CAPE is not significantly increased compared to warm fronts that are primarily associated with condensation (not shown).

3.4.3 The cyclone center

The positive PV anomaly in the cyclone center is primarily generated by condensation, convection, and turbulent momentum tendencies (Fig. 4a, third panel). All three classes of cyclones are approximately equally intense (see SLP contours in Fig. 9a,f,k). Cyclones associated with PV generation by convection cluster  the western ocean basis whereas those associated with turbulent momentum tendencies frequently occur over land (Fig. 6c).

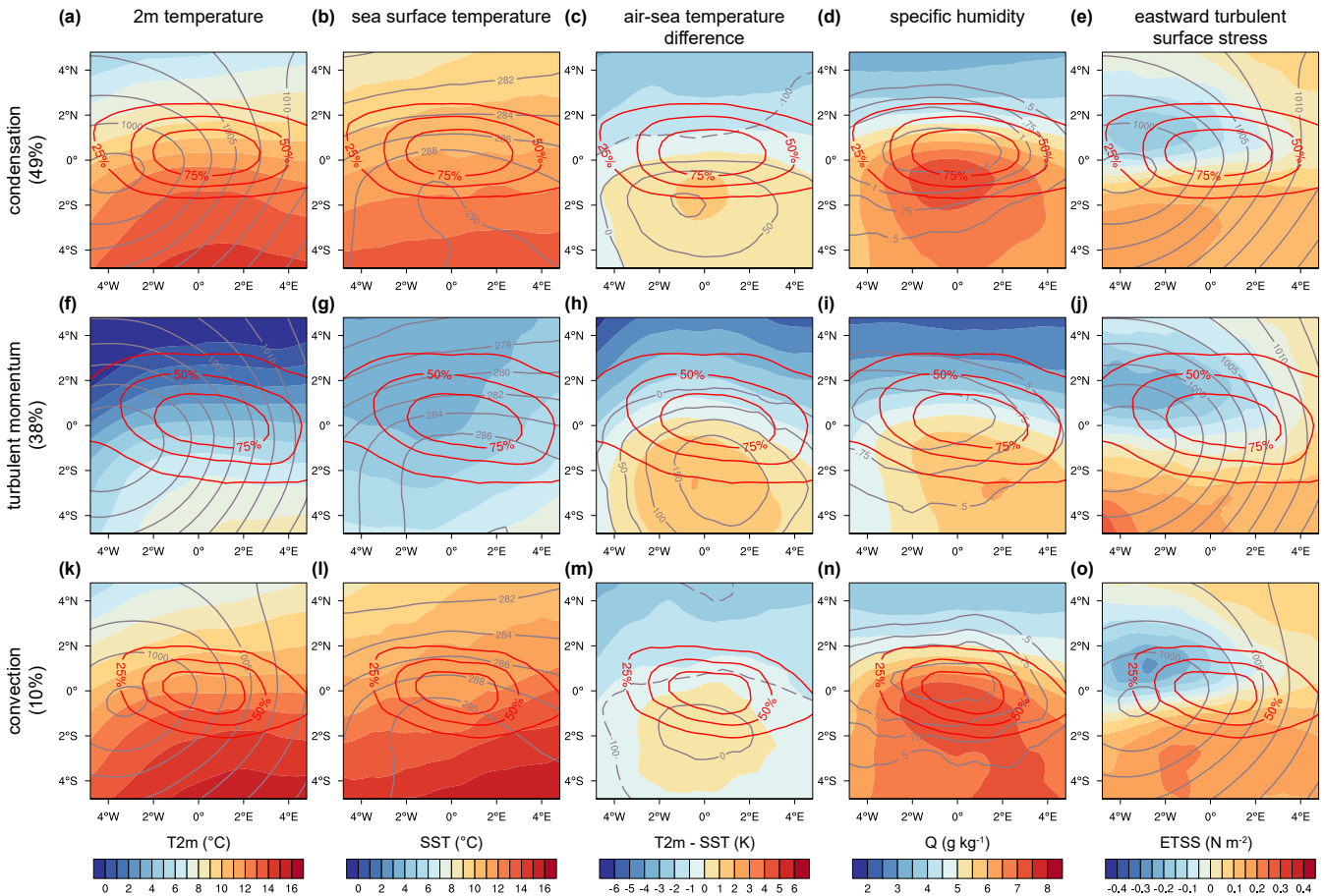


Figure 8. Similar to Fig. 7, but for the positive PV anomaly along the warm front in the cold season. Gray contours show sea level pressure (first and last column), θ on 900 hPa (second column), surface sensible heat flux (third column), and total precipitation (fourth column).

The first row of Fig. 9 shows the environment of cyclones that mainly experience PV generation by condensation. In line with our previous findings, these cyclones are characterized by high specific humidity and intense large-scale precipitation (not shown). Further, we find that the air in the cold sector is colder than the ocean, whereas the warm sector is warmer than the underlying ocean (Fig. 9c). This leads to heating of the boundary layer in the cold sector and cooling in the warm sector, associated with long-wave radiative heating and cooling as well as negative and positive PV generation, respectively (not shown).

Cyclones that primarily experience PV generation by convection occur over warmer SSTs (Fig. 9g). This leads to a negative air-sea temperature difference throughout the entire warm sector (Fig. 9h), which is associated with SSHF directed into the atmosphere. This likely leads to the destabilization of the boundary layer inducing convection. In contrast to convection-dominated cold fronts, which are associated with enhanced CAPE (Fig. 7j), no significant increase in CAPE was found for the cyclone center (not shown). However, higher wind speeds are observed for this type of cyclones (Fig. 9j), in line with the more

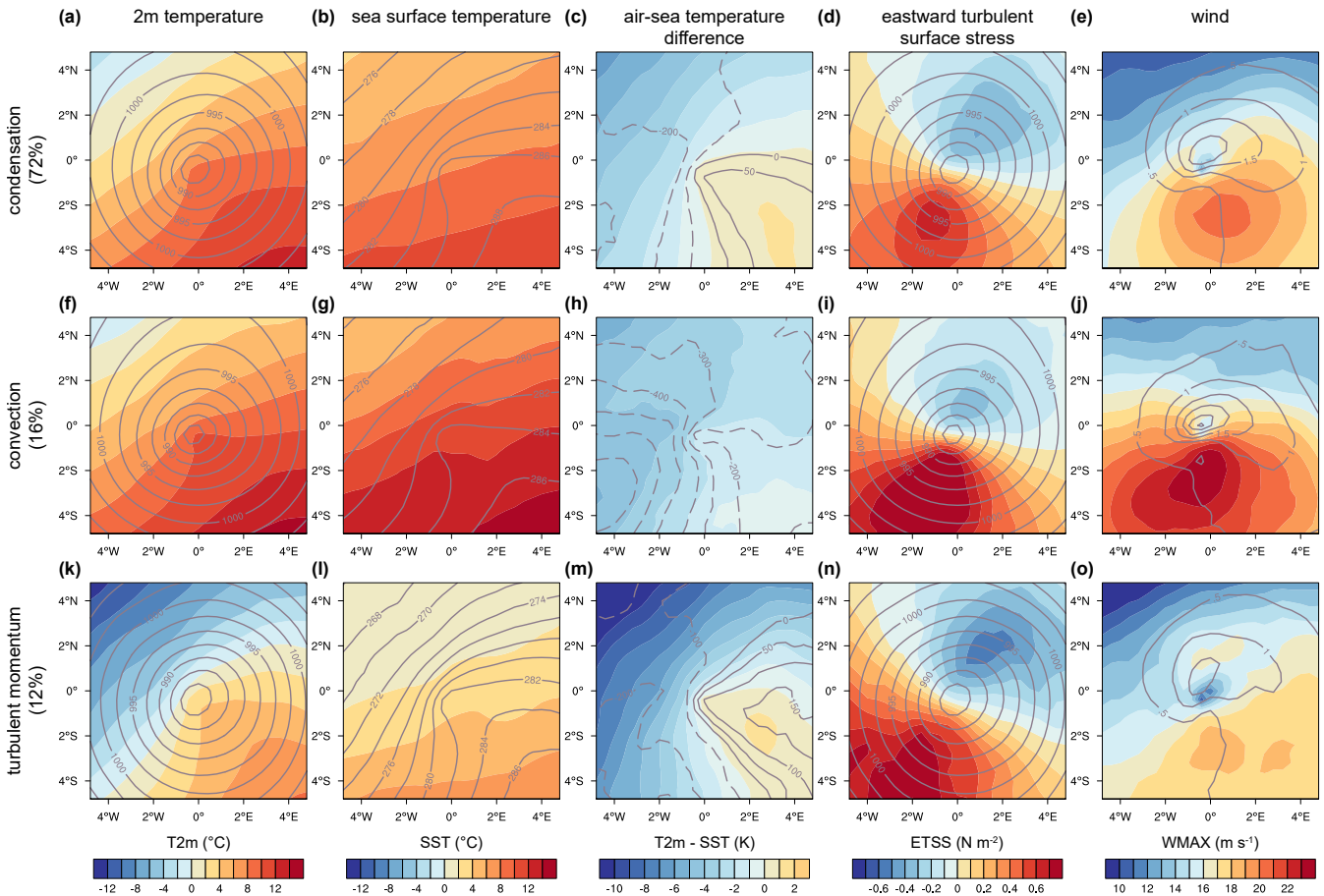


Figure 9. Similar to Fig. 7, but for the positive PV anomaly in the cyclone center in the cold season. Gray contours show sea level pressure (first and fourth column), θ on 900 hPa (second column), surface sensible heat flux (third column), and total precipitation (last column).

intense PV anomaly generated by convection compared to the other processes (Fig. 4a, third panel). Finally, these cyclones produce a much more intense and focused area of precipitation (contours in Fig. 9j).

The final row of Fig. 9 shows composites of cyclones whose central positive PV anomaly is mainly generated by turbulent momentum tendencies. Generally, the environment of these cyclones is similar to the warm fronts that belong in this category (Fig. 8, second row). They occur at markedly lower surface and sea surface temperatures (Fig. 9k, l) characterized by a positive air-sea temperature difference in the warm sector (Fig. 9m) linked to positive SSHF. Strong negative ETSS occurs along the warm front in a region with a strong negative meridional θ gradient (Fig. 9n). As described for the warm front, this leads to turbulent PV generation. Finally, this type of cyclone is associated with only weak surface winds and comparatively little precipitation (Fig. 9o).



4 Conclusions

This paper provides an overview of the relevance of different diabatic processes for the generation of low-level PV anomalies in 288 rapidly intensifying extratropical cyclones. Results are based on a series of twelve 35-day model simulations initialized from ECMWF analyses on the first day of the month from December 2017 until November 2018. Simulations are performed using a modified version of the IFS cycle 43R1 from the ECMWF, similar to Spreitzer et al. (2019) and Attinger et al. (2019). The 24 most rapidly intensifying extratropical cyclones from each month are selected and results are split into an extended cold (from October to March) and warm season from April to September).

Hourly PV tendencies of each parametrized process are calculated from individual heating and momentum tendencies obtained from the model following Eq. (1). As instantaneous PV tendencies are often susceptible to large cancellation and are quickly advected by the flow, this investigation considers their integrated effect along air parcel trajectories following the approach introduced by Joos and Forbes (2016) and refined by Crezee et al. (2017). Thereby, the influence of individual diabatic processes for the generation of PV anomalies can be computed by accumulating PV tendencies along backward trajectories. This study focuses on positive PV anomalies ($PV \geq 1$ PVU) along the cold front, warm front, and in the cyclone center as well as negative PV anomalies ($PV \leq -0.1$ PVU) along the cold front and warm front.

Generally, we found that using integrated hourly PV tendencies along backward trajectories based on temperature and momentum tendencies from the model parametrization works well to quantify the processes that modify PV along frontal features of extratropical cyclones. The selection of 15 h instead of the longer 24 h backward trajectories used in previous studies (Crezee et al., 2017; Spreitzer et al., 2019; Attinger et al., 2019) resulted in a slightly smaller residual while still retaining information on the relevant processes that dominate the PV budget.

The selected extratropical cyclones primarily occur in the storm track during the cold season (Fig. 1a). Conversely, a large fraction of continental cyclones are considered during the warm season (Fig. 1b). On average, both positive (1.8 vs 1.64 PVU) and negative (-0.38 vs. -0.34 PVU) PV anomalies are more intense in the warm season compared to the cold season (Table 4). While positive PV anomalies are also large in the warm season (1.4×10^5 vs 1.3×10^5 km²), negative PV anomalies are large in the cold season (1.9×10^5 vs 2.6×10^5 km²). Positive PV anomalies are located on average higher (44.8 hPa) than negative PV anomalies (970.8 hPa) with a slight tendency for lower elevations in the warm season.

Contributions of different processes to PV anomalies remain temporally largely consistent when averaging them over all cyclones of one season (Fig. 3a). However, a large case-to-case variability is found when comparing contributions across individual cyclones (Fig. 3b). To account for this variability, processes are ranked according to their area-weighted mean contribution to the different PV anomalies. This enables the computation of the fraction of cyclones with a specific process as the most dominant for the generation of a given PV anomaly.

The positive PV anomaly at the cold front is primarily generated by condensation (53% of cyclones), convection (29%), and long-wave radiative cooling (14%) in the cold season (Fig. 4a). Condensation is again found to be the dominant process in the warm season (55% of cyclones), whereas long-wave radiative cooling (20%) becomes more important than convection (9%, Fig. 5a). Environmental composites of the cold fronts associated with convection as the most important process during



the cold season reveal a negative air-sea temperature difference in the warm sector (Fig. 7h). This is associated with negative SSHF (i.e. heating of the atmosphere) which destabilizes the boundary layer. During the warm season, only few cases are dominated by convection (Fig. 5a) because negative air-sea temperature differences are rarely achieved (not shown). Cyclones associated with PV generation by long-wave radiative cooling at the cold front primarily occur at higher latitudes and in a colder environment than the other two categories (Fig. 6a). This process stabilizes the boundary layer and thereby increases PV in the vicinity of the cold front where relative vorticity is enhanced, corroborating the findings of Neiman et al. (1990). Additionally, the reduced moisture capacity of colder air (Fig. 7n) reduces the importance of condensation for the generation of PV in those cyclones.

Negative PV anomalies west of the cold front are primarily generated by turbulent momentum tendencies (46%), long-wave radiative heating (39%), and turbulent temperature tendencies (14%) during the cold season (Fig. 4b). Turbulent momentum tendencies (58%) remain the dominant process decreasing PV along the cold front in the warm season (Fig. 5b), whereas an increased fraction of cyclones experiences turbulent temperature tendencies (18%) and a reduced fraction is associated with long-wave radiative heating (18%). The latter is likely due to the higher 2 m temperatures in the warm season. The generation of negative PV in the cold sector by the destabilization of the boundary layer by surface fluxes was previously described by Chagnon et al. (2013) for a single case study and Vanni re et al. (2016) using ERA-Interim reanalysis data, respectively.

Condensation increases PV along the warm front in 49% of all cyclones during the cold season, followed by turbulent momentum tendencies (38%), and convection (10%). Conversely, turbulent mixing of momentum becomes the dominant process in 54% of all cyclones during the warm season, with condensation and convection reduced to 39% and 3%, respectively. Cyclones associated with PV generation by turbulent momentum tendencies at the warm front primarily occur over land (Fig. 6b). Hence, their prevalence increases in the warm season. More specifically, a region of eastward acceleration of the prevailing easterly flow north of the warm front was found to be responsible for the generation of PV in a highly baroclinic environment (Fig. 8j). The importance of turbulence for the generation of PV along the warm front is in line with the findings of previous research (Adamson et al., 2006; Plant and Belcher, 2007; Vanni re et al., 2016).

Negative PV anomalies along the warm front are produced by long-wave radiative heating (38%), turbulent momentum tendencies (22%), and melting of snow (21%) in the cold season (Fig. 4b). The reduction of PV by snow sublimation north of the warm front supports previous studies that investigated the diabatic PV modification in an idealized simulation (Crezee et al., 2017) and in a Pacific cyclone (Attinger et al., 2019). Long-wave radiative heating no longer appears as one of the three most relevant processes to produce negative PV anomalies at the warm front in the warm season (Fig. 5b), with turbulent temperature tendencies (50%), melting of snow (14%), and turbulent temperature tendencies (4%) becoming more dominant. The shift towards stronger importance of turbulence in the PV budget is likely due to the larger number of continental cyclones in the warm season compared to the cold season (Fig. 1).

The generation of PV in the cyclone center and along the bent-back front is dominated by condensation accounting for 71% and 77% of all cyclones during the cold and warm season, respectively. A larger fraction of cyclones associated with convection during the cold season (16%) than in the warm season (5%) due to the required negative air-sea temperature



difference (Fig. 9h). Finally, turbulent momentum tendencies generate the positive PV anomaly in the cyclone center in 12%
475 (16%) of all cyclones during the cold (warm) season.

While condensation and convection are often described as the main processes responsible for the generation of positive PV anomalies in extratropical cyclones (e.g. Ahmadi-Givi, 2002), we show that other processes such as turbulent momentum tendencies or long-wave radiative cooling can be equally or even more important than condensation in selected cases. Moreover, turbulent temperature tendencies partially offset the generation of PV whenever the PV budget is strongly affected by processes
480 related to diabatic heating or cooling. For the generation of negative PV anomalies, we highlight the relevance of long-wave radiative heating, turbulence, and melting of snow. The results presented here also corroborate recent research highlighting the sensitivity of NWP models to the correct representation of microphysical processes (Forbes and Clark, 2003; Martínez-Alvarado and Plant, 2014; Dearden et al., 2016).

Although this study provides a first overview of the different diabatic processes that modify PV in a large number of rapidly
485 intensifying extratropical cyclones, additional work is required to further generalize the findings presented here with respect to other NWP models, different parametrization schemes, and a larger range of different cyclone types and intensities. Moreover, it will be relevant to assess the direct and indirect dynamical impact of the different PV anomalies, similar to the recent study of Oertel and Schemm (2021).

Author contributions. RA developed the evaluation framework, assessed the data, and wrote the paper with contributions from HJ, HW, and
490 MB. ES ran the model simulations and supported the evaluation of the data. HJ and HW wrote the project proposal leading to the funding of this study. All co-authors commented on and helped improving the manuscript.

Competing interests. Heini Wernli is executive editor and co-editor of WCD.

Acknowledgements. RA and MB received funding from the Swiss National Science Foundation (Project 165941), and MB from the European Research Council, H2020 research and innovation program (INTEXseas, grant no. 787652). This work is part of the ECMWF special
495 project "Diabatic effects in mid-latitude weather systems". We acknowledge MeteoSwiss and ECMWF for access to the ECMWF computing facilities. We thank Carsten Maass and Richard Forbes for their support with running the IFS simulations and Michael Sprenger for this help with LAGRANTO.



References

- Adamson, D., Belcher, S. E., Hoskins, B. J., and Plant, R. S.: Boundary-layer friction in midlatitude cyclones, *Q. J. R. Meteorol. Soc.*, 132,
 101–124, <https://doi.org/10.1256/qj.04.145>, 2006.
- Aebischer, U. and Schär, C.: Low-level potential vorticity and cyclogenesis to the lee of the Alps, *J. Atmos. Sci.*, 55, 186–207,
[https://doi.org/10.1175/1520-0469\(1998\)055<0186:LLPVAC>2.0.CO;2](https://doi.org/10.1175/1520-0469(1998)055<0186:LLPVAC>2.0.CO;2), 1998.
- Ahmadi-Givi, F.: A review of the role of latent heat release in extratropical cyclones within potential vorticity framework, *J. Earth Space
 Phys.*, 28, 7–20, 2002.
- Attinger, R.: Quantifying the diabatic modification of potential vorticity in extratropical cyclones, Ph.D. thesis, Swiss federal institute of
 technology Zurich, <https://doi.org/10.3929/ethz-b-000432253>, 2020.
- Attinger, R., Spreitzer, E., Boettcher, M., Forbes, R., Wernli, H., and Joos, H.: Quantifying the role of individual diabatic processes for the
 formation of PV anomalies in a North Pacific cyclone, *Q. J. R. Meteorol. Soc.*, 145, 2454–2476, <https://doi.org/10.1002/qj.3573>, 2019.
- Beare, R. J.: Boundary layer mechanisms in extratropical cyclones, *Q. J. R. Meteorol. Soc.*, 133, 503–515, <https://doi.org/10.1002/qj.30>,
 2007.
- Binder, H., Boettcher, M., Joos, H., and Wernli, H.: The role of warm conveyor belts for the intensification of extratropical cyclones in
 Northern Hemisphere winter, *J. Atmos. Sci.*, 73, 3997–4020, <https://doi.org/10.1175/JAS-D-15-0302.1>, 2016.
- Boutle, I., Belcher, S. E., and Plant, R.: Friction in mid-latitude cyclones: an Ekman-PV mechanism, *Atmos. Sci. Lett.*, 16, 103–109,
<https://doi.org/10.1002/asl2.526>, 2015.
- Browning, K., Hardman, M., Harrold, T., and Pardoe, C.: The structure of rainbands within a mid-latitude depression, *Q. J. R. Meteorol.
 Soc.*, 99, 215–231, <https://doi.org/10.1002/qj.49709942002>, 1973.
- Browning, K. A.: Organization of clouds and precipitation in extratropical cyclones, pp. 129–153, *Amer. Meteor. Soc.*,
https://doi.org/10.1007/978-1-944970-33-8_8, 1990.
- Chagnon, J., Gray, S., and Methven, J.: Diabatic processes modifying potential vorticity in a North Atlantic cyclone, *Q. J. R. Meteorol. Soc.*,
 139, 1270–1282, <https://doi.org/10.1002/qj.2037>, 2013.
- Crezee, B., Joos, H., and Wernli, H.: The microphysical building blocks of low-level potential vorticity anomalies in an idealized extratropical
 cyclone, *J. Atmos. Sci.*, 74, 1403–1416, <https://doi.org/10.1175/JAS-D-16-0260.1>, 2017.
- Davis, C. A.: A potential-vorticity diagnosis of the importance of initial structure and condensational heating in observed extratropical
 cyclogenesis, *Mon. Wea. Rev.*, 120, 2409–2428, [https://doi.org/10.1175/1520-0493\(1992\)120<2409:APVDOT>2.0.CO;2](https://doi.org/10.1175/1520-0493(1992)120<2409:APVDOT>2.0.CO;2), 1992.
- Davis, C. A. and Emanuel, K. A.: Potential vorticity diagnostics of cyclogenesis, *Mon. Wea. Rev.*, 119, 1929–1953,
[https://doi.org/10.1175/1520-0493\(1991\)119<1929:PVDOC>2.0.CO;2](https://doi.org/10.1175/1520-0493(1991)119<1929:PVDOC>2.0.CO;2), 1991.
- Dearden, C., Vaughan, G., Tsai, T., and Chen, J.-P.: Exploring the diabatic role of ice microphysical processes in two North Atlantic summer
 cyclones, *Mon. Wea. Rev.*, 144, 1249–1272, <https://doi.org/10.1175/MWR-D-15-0253.1>, 2016.
- Ertel, H.: Ein neuer hydrodynamischer Wirbelsatz, *Meteor. Z.*, 9, 271–281, 1942.
- Fink, A. H., Pohle, S., Pinto, J. G., and Knippertz, P.: Diagnosing the influence of diabatic processes on the explosive deepening of extratropical
 cyclones, *Geophys. Res. Lett.*, 39, <https://doi.org/10.1029/2012GL051025>, 2012.
- Forbes, R. M. and Clark, P. A.: Sensitivity of extratropical cyclone mesoscale structure to the parametrization of ice microphysical processes,
Q. J. R. Meteorol. Soc., 129, 1123–1148, <https://doi.org/10.1256/qj.01.171>, 2003.



- Green, J., Ludlam, F., and McIlveen, J.: Isentropic relative-flow analysis and the parcel theory, *Q. J. R. Meteorol. Soc.*, 92, 210–219,
 535 <https://doi.org/10.1002/qj.49709239204>, 1966.
- Hardy, S., Schultz, D. M., and Vaughan, G.: Early evolution of the 23–26 September 2012 UK floods: Tropical Storm Nadine and diabatic heating due to cloud microphysics, *Mon. Wea. Rev.*, 145, 543–563, <https://doi.org/10.1175/MWR-D-16-0200.1>, 2017.
- Harrold, T.: Mechanisms influencing the distribution of precipitation within baroclinic disturbances, *Q. J. R. Meteorol. Soc.*, 99, 232–251, <https://doi.org/10.1002/qj.49709942003>, 1973.
- 540 Hoskins, B. J., McIntyre, M., and Robertson, A. W.: On the use and significance of isentropic potential vorticity maps, *Q. J. R. Meteorol. Soc.*, 111, 877–946, <https://doi.org/10.1002/qj.49711147002>, 1985.
- Huang, H.-C. and Emanuel, K. A.: The effects of evaporation on frontal circulations, *J. Atmos. Sci.*, 48, 619–628, [https://doi.org/10.1175/1520-0469\(1991\)048<0619:TEOEOF>2.0.CO;2](https://doi.org/10.1175/1520-0469(1991)048<0619:TEOEOF>2.0.CO;2), 1991.
- Igel, A. L. and v. d. Heever, S. C.: The role of latent heating in warm frontogenesis, *Q. J. R. Meteorol. Soc.*, 140, 139–150,
 545 <https://doi.org/10.1002/qj.2118>, 2014.
- Joos, H. and Forbes, R.: Impact of different IFS microphysics on a warm conveyor belt and the downstream flow evolution, *Q. J. R. Meteorol. Soc.*, 142, 2727–2739, <https://doi.org/10.1002/qj.2863>, 2016.
- Joos, H. and Wernli, H.: Influence of microphysical processes on the potential vorticity development in a warm conveyor belt: A case-study with the limited-area model COSMO, *Q. J. R. Meteorol. Soc.*, 138, 407–418, 2012.
- 550 Kuo, Y.-H., Shapiro, M., and Donall, E. G.: The interaction between baroclinic and diabatic processes in a numerical simulation of a rapidly intensifying extratropical marine cyclone, *Mon. Wea. Rev.*, 119, 368–384, [https://doi.org/10.1175/1520-0493\(1991\)119<0368:TIBBAD>2.0.CO;2](https://doi.org/10.1175/1520-0493(1991)119<0368:TIBBAD>2.0.CO;2), 1991.
- Lackmann, G. M.: Cold-frontal potential vorticity maxima, the low-level jet, and moisture transport in extratropical cyclones, *Mon. Wea. Rev.*, 130, 59–74, [https://doi.org/10.1175/1520-0493\(2002\)130<0059:CFPVM>2.0.CO;2](https://doi.org/10.1175/1520-0493(2002)130<0059:CFPVM>2.0.CO;2), 2002.
- 555 Lackmann, G. M. and Yablonsky, R. M.: The importance of the precipitation mass sink in tropical cyclones and other heavily precipitating systems, *J. Atmos. Sci.*, 61, 1674–1692, [https://doi.org/10.1175/1520-0469\(2004\)061<1674:TIOTPM>2.0.CO;2](https://doi.org/10.1175/1520-0469(2004)061<1674:TIOTPM>2.0.CO;2), 2004.
- Manabe, S.: On the contribution of heat released by condensation to the change in pressure pattern, *J. Meteor. Soc. Japan*, 34, 308–320, https://doi.org/10.2151/jmsj1923.34.6_308, 1956.
- Martínez-Alvarado, O. and Plant, R.: Parametrized diabatic processes in numerical simulations of an extratropical cyclone, *Q. J. R. Meteorol. Soc.*, 140, 1742–1755, <https://doi.org/10.1002/qj.2254>, 2014.
 560
- Muir, L. C. and Reeder, M. J.: Idealized modelling of landfalling cold fronts, *Q. J. R. Meteorol. Soc.*, 136, 2147–2161, <https://doi.org/10.1002/qj.692>, 2010.
- Neiman, P. J. and Shapiro, M.: The life cycle of an extratropical marine cyclone. Part I: Frontal-cyclone evolution and thermodynamic air-sea interaction, *Mon. Wea. Rev.*, 121, 2153–2176, [https://doi.org/10.1175/1520-0493\(1993\)121<2153:TLCOAE>2.0.CO;2](https://doi.org/10.1175/1520-0493(1993)121<2153:TLCOAE>2.0.CO;2), 1993.
- 565 Neiman, P. J., Shapiro, M., Donall, E. G., and Kreitzberg, C. W.: Diabatic modification of an extratropical marine cyclone warm sector by cold underlying water, *Mon. Wea. Rev.*, 118, 1576–1590, [https://doi.org/10.1175/1520-0493\(1990\)118<1576:DMOAE>2.0.CO;2](https://doi.org/10.1175/1520-0493(1990)118<1576:DMOAE>2.0.CO;2), 1990.
- Oertel, A. and Schemm, S.: Quantifying the circulation induced by convective clouds in kilometer-scale simulations, *Q. J. R. Meteorol. Soc.*, 147, 1752–1766, <https://doi.org/10.1002/qj.3992>, 2021.
- 570 Parfitt, R., Czaja, A., and Seo, H.: A simple diagnostic for the detection of atmospheric fronts, *Geophys. Res. Lett.*, 44, 4351–4358, <https://doi.org/10.1002/2017GL073662>, 2017.



- Plant, R. and Belcher, S.: Numerical simulation of baroclinic waves with a parameterized boundary layer, *J. Atmos. Sci.*, 64, 4383–4399, <https://doi.org/10.1175/2007JAS2269.1>, 2007.
- 575 Rodwell, M. J., Magnusson, L., Bauer, P., Bechtold, P., Bonavita, M., Cardinali, C., Diamantakis, M., Earnshaw, P., Garcia-Mendez, A., Isaksen, L., et al.: Characteristics of occasional poor medium-range weather forecasts for Europe, *Bull. Amer. Meteor. Soc.*, 94, 1393–1405, <https://doi.org/10.1175/BAMS-D-12-00099.1>, 2013.
- Rossby, C.: Planetary flow patterns in the atmosphere, *Quart. J. Roy. Met. Soc.*, 66, 68, 1940.
- Saffin, L., Methven, J., and Gray, S.: The non-conservation of potential vorticity by a dynamical core compared with the effects of parametrized physical processes, *Q. J. R. Meteorol. Soc.*, 142, 1265–1275, <https://doi.org/10.1002/qj.2729>, 2016.
- 580 Sanders, F. and Gyakum, J. R.: Synoptic-dynamic climatology of the “bomb”, *Mon. Wea. Rev.*, 108, 1589–1606, [https://doi.org/10.1175/1520-0493\(1980\)108<1589:SDCOT>2.0.CO;2](https://doi.org/10.1175/1520-0493(1980)108<1589:SDCOT>2.0.CO;2), 1980.
- Spreitzer, E., Attinger, R., Boettcher, M., Forbes, R., Wernli, H., and Joos, H.: Modification of potential vorticity near the tropopause by non-conservative processes in the ECMWF model, *J. Atmos. Sci.*, 76, 1709–1726, <https://doi.org/10.1175/JAS-D-18-0295.1>, 2019.
- Sprenger, M. and Wernli, H.: The LAGRANTO Lagrangian analysis tool–version 2.0, *Geosci. Model Dev.*, 8, 2569–2586, <https://doi.org/10.5194/gmd-8-2569-2015>, 2015.
- 585 Stoelinga, M. T.: A potential vorticity-based study of the role of diabatic heating and friction in a numerically simulated baroclinic cyclone, *Mon. Wea. Rev.*, 124, 849–874, [https://doi.org/10.1175/1520-0493\(1996\)124<0849:APVBSO>2.0.CO;2](https://doi.org/10.1175/1520-0493(1996)124<0849:APVBSO>2.0.CO;2), 1996.
- Szeto, K. and Stewart, R.: Effects of melting on frontogenesis, *J. Atmos. Sci.*, 54, 689–702, [https://doi.org/10.1175/1520-0469\(1997\)054<0689:EOMOF>2.0.CO;2](https://doi.org/10.1175/1520-0469(1997)054<0689:EOMOF>2.0.CO;2), 1997.
- 590 Tory, K. J. and Reeder, M. J.: The effect of the continental boundary layer on the dynamics of fronts in a 2D model of baroclinic instability. I: An insulated lower surface, *Q. J. R. Meteorol. Soc.*, 131, 2389–2408, <https://doi.org/10.1256/qj.04.26>, 2005.
- Valdes, P. J. and Hoskins, B. J.: Baroclinic instability of the zonally averaged flow with boundary layer damping, *J. Atmos. Sci.*, 45, 1584–1593, [https://doi.org/10.1175/1520-0469\(1988\)045<1584:BIOTZA>2.0.CO;2](https://doi.org/10.1175/1520-0469(1988)045<1584:BIOTZA>2.0.CO;2), 1988.
- Vannière, B., Czaja, A., Dacre, H., Woollings, T., and Parfitt, R.: A potential vorticity signature for the cold sector of winter extratropical cyclones, *Q. J. R. Meteorol. Soc.*, 142, 432–442, <https://doi.org/10.1002/qj.2662>, 2016.
- 595 Vaughan, G., Methven, J., Anderson, D., Antonescu, B., Baker, L., Baker, T., Ballard, S., Bower, K., Brown, P., Chagnon, J., et al.: Cloud banding and winds in intense European cyclones: Results from the DIAMET project, *Bull. Amer. Meteor. Soc.*, 96, 249–265, <https://doi.org/10.1175/BAMS-D-13-00238.1>, 2015.
- Wernli, H. and Davies, H. C.: A Lagrangian-based analysis of extratropical cyclones. I: The method and some applications, *Q. J. R. Meteorol. Soc.*, 123, 467–489, <https://doi.org/10.1002/qj.49712353811>, 1997.
- 600 Wernli, H. and Schwierz, C.: Surface cyclones in the ERA-40 dataset (1958–2001). Part I: Novel identification method and global climatology, *J. Atmos. Sci.*, 63, 2486–2507, <https://doi.org/10.1175/JAS3766.1>, 2006.
- Willison, J., Robinson, W. A., and Lackmann, G. M.: The importance of resolving mesoscale latent heating in the North Atlantic storm track, *J. Atmos. Sci.*, 70, 2234–2250, <https://doi.org/10.1175/JAS-D-12-0226.1>, 2013.